Modeling Hydrodynamic and Biomass Pyrolysis Effects of Recycled Product Gases in a Bubbling Fluidized Bed Reactor

Gavin M. Wiggins, Oluwafemi A. Oyedeji, and Zachary G. Mills

February 18, 2022

Abstract

Fast pyrolysis of biomass in a fluidized bed reactor is typically conducted in a nitrogen gas environment. Recycling product gas can improve the economics of operating such a system by reducing reliance on pure process streams. Gas effects in a fluidized bed biomass pyrolysis reactor using engineering correlations, low-order models, and CFD simulations were investigated for N_2, H_2, CO, CO_2, and CH_4 carrier gas mixtures. Our findings reveal viscosity of a gas mixture can be significantly underestimated depending on the model. Furthermore, fluidization characteristics such as U_{mf} and gas-solid convective heat transfer can be greatly affected by the gas properties. By utilizing a low molecular weight gas such as H_2 while maintaining a constant U_s/U_{mf}, the bio-oil yields can be increased 7.7%. This is due to the lower density H_2 producing similar hydrodynamics as N_2 at higher gas flow rates. These higher flow rates result in shorter gas residence times, and as a result, less secondary reactions that convert bio-oil to light gases and char.

1 Introduction

Fast pyrolysis is a versatile method for thermochemical conversion of solid biomass into liquid bio-oil which can be used for bio-fuel and high-value chemical production. Bio-oil is commonly generated in bubbling fluidized bed and circulating fluidized bed reactor systems in which biomass particles rapidly devolatilize in the absence of oxygen into mixtures of light gases, condensable bio-oil vapors, and solid char [4, 5, 25]. Since biomass pyrolysis normally occurs in a non-oxidizing environment, the fluidization gas (carrier gas) is often pure nitrogen [25]. To maximize bio-oil yields, the reactor typically operates at temperatures near 500°C and must maintain particle residence times up to 10 seconds and gas residence times less than 2 seconds [5]. Deviations from these conditions can result in significant production and quality penalties; therefore,

optimal reactor design and control become crucial to achieving commercially viable bio-oil production.

To improve the economic feasibility of biomass fast pyrolysis systems, char can be burned for process heat while recycled pyrolysis gas can assist with fluidization [4, 23, 10]. The major generated components of pyrolysis gas are CO, CO_2, CH_4, H_2, along with other light hydrocarbons [1, 41]. Several experiments investigated the effects of these gases on reactor conditions and pyrolysis yields [23, 26, 41, 10] but modeling the effects of the different gases was not discussed.

Autothermal pyrolysis experiments in a fluidized bed reactor has shown that the presence of oxygen in the carrier gas can prevent reactor clogging by reducing char formation [19]. The addition of oxygen can also improve heat transfer within the reactor via partial oxidiation of the pyrolysis products without significant decreases in bio-oil yield [32]. Substituting air for nitrogen gas allowed for higher superficial velocities which promoted elutriation of char from reactor experiments while having neglible effect on bio-oil yield [31]. Modeling the fluidization of the autothermal experiments was not discussed in the available literature.

There are several fluidized bed reactor models that investigate the hydrodynamics and conversion of biomass at fast pyrolysis conditions [30, 29, 24, 38, 39]. These models assume the carrier gas is pure nitrogen which is a typical scenario for biomass fast pyrolysis. We are not aware of any models in the biomass pyrolysis literature that investigate the effects of a carrier gas other than pure nitrogen. Consequently, our objective in this paper is to evaluate different fluidization gases and their effects on the hydrodynamics and biomass conversion in a bubbling fluidized bed reactor operating at fast pyrolysis conditions. The effects on the pyrolysis reaction chemistry are not accounted for in this work. Our methodology uses engineering correlations, reducing-order modeling techniques, and CFD simulations to model these effects and compare the model results (where applicable) to experimental data.

2 Experimental apparatus

The NREL 2FBR reactor system thermochemically converts biomass feedstock at fast pyrolysis conditions. The system is comprised of two bubbling fluidized bed (BFB) reactors where the first reactor is a biomass fast pyrolysis unit (also known as the "pyrolyzer") and the second reactor is for vapor phase upgrading. An overview of the components and inlet/outlet flows of the NREL 2FBR pyrolysis unit is shown in Figure 1, while dimensions and typical operating conditions of the pyrolysis reactor are detailed in Figure 2. Sand along with the carrier gas is used as the fluidization medium in the pyrolyzer while biomass particles are fed to the reactor via a screw auger. More information about the NREL 2FBR biomass pyrolysis system is available elsewhere [17, 36]. Yields from the BFB pyrolysis reactor are compared to model results discussed later in this paper.
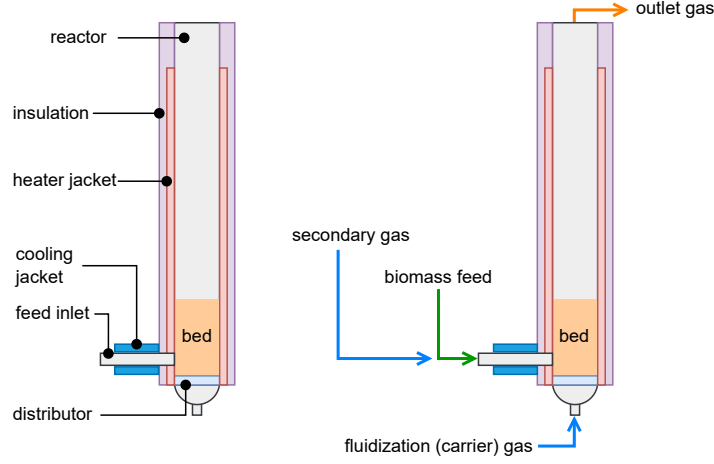
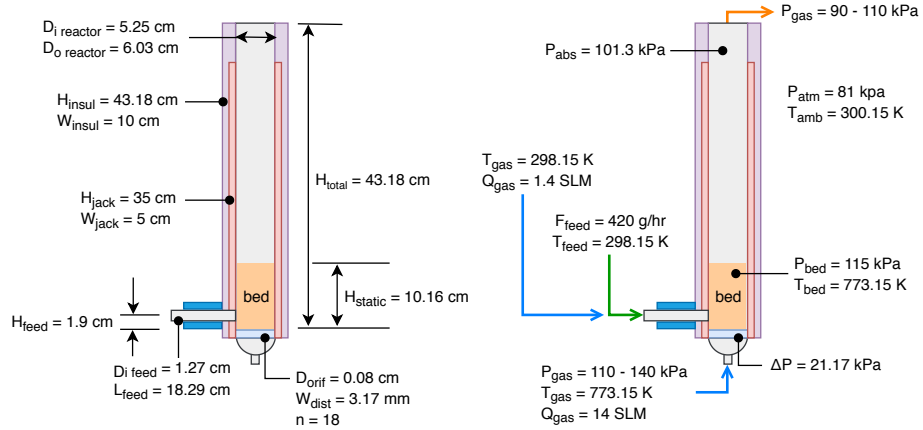Figure 1: Components and inlet/outlet flows of the BFB biomass pyrolysis reactor in the NREL 2FBR system.

Figure 2: Dimensions and typical fast pyrolysis operating conditions for the BFB biomass pyrolysis reactor in the NREL 2FBR system.

3   Modeling approach

Our strategy to model gas effects in a bubbling fluidized bed reactor begins with determining gas properties such as density, dynamic viscosity, thermal conductivity, and heat capacity. Once the individual gas viscosity is known, the viscosity of a gas mixture is calculated using various mixture models. Next, fluidization correlations relevant to fluidized bed reactors are used to investigate the effects of the gas properties on the hydrodynamics of the system. Dimen-

sionless numbers provide insight on the limiting mechanisms in regards to the pyrolysis of the biomass particles. Finally, CFD-DEM simulations provide residence times and product yields related to the different carrier gas scenarios.

3.1 Gas properties

Gas density is calculated using the ideal gas law as shown in Equation 1 where ρ_{gas} is density ($\mathrm{kg/m^3}$), P is pressure (Pa), M is molecular weight (g/mol), R is the gas constant ($\mathrm{m^3 \cdot Pa}$ / $\mathrm{K \cdot mol}$), and T is temperature (K).

$$\rho_{\mathrm{gas}} = \frac{P\,M}{R\,T} \tag{1}$$

Dynamic gas viscosity μ_{gas} is estimated by Equation 2 in units of µP. Gas thermal conductivity k_{gas} as $\mathrm{W/m \cdot K}$ is calculated from Equation 3 and heat capacity $C_{\mathrm{p\,gas}}$ as $\mathrm{J/mol \cdot K}$ is determined using Equation 4. In each equation, temperature is denoted by T in units of Kelvin while the regression coefficients A, B, C, D, E, F, and G for a particular gas were obtained from Yaws' Handbook [40].

$$\mu_{\mathrm{gas}} = A + B\,T + C\,T^2 + D\,T^3 \tag{2}$$

$$k_{\mathrm{gas}} = A + B\,T + C\,T^2 + D\,T^3 \tag{3}$$

$$C_{\mathrm{p\,gas}} = A + B\,T + C\,T^2 + D\,T^3 + E\,T^4 + F\,T^5 + G\,T^6 \tag{4}$$

Several methods are available to calculate the dynamic viscosity of a gas mixture. The simplest approach is Graham's model in Equation 5 which sums the gas viscosities μ_i and mole fractions x_i of each gas component [14].

$$\mu_{\mathrm{mix}} = \sum (x_i\,\mu_i) \tag{5}$$

The Herning and Zipperer approach shown by Equation 6, sums the viscosities weighted by the square root of the molecular weight M_i for each component [16]. According to Davidson's report [9], the Herning and Zipperer model is not recommended for gas mixtures containing significant amounts of hydrogen.

$$\mu_{\mathrm{mix}} = \sum \frac{\mu_i\,x_i\,\sqrt{M_i}}{x_i\,\sqrt{M_i}} \tag{6}$$

Wilke's model represented by Equations 7 and 8 is based on a kinetic theory implementation which requires a coefficient ϕ_{ij} for each gas component [37]. The coefficients are used along with the mole fractions to calculate the overall mixture viscosity.

$$\phi_{ij} = \frac{\left[1 + (\mu_i/\mu_j)^{1/2}(M_j/M_i)^{1/4}\right]^2}{(4/\sqrt{2})\left[1 + (M_i/M_j)\right]^{1/2}} \tag{7}$$

$$\mu_{\text{mix}} = \sum_{i=1} \frac{\mu_i}{1 + \frac{1}{x_i}\sum_{\substack{j=1 \\ j \neq i}} x_j\,\phi_{ij}} \tag{8}$$

Brokaw provides a model for nonpolar and polar gas mixtures that utilizes the viscosities, molecular weights, and mole fractions of the mixture components [6]. The molecular weight ratios of the gas components are described by Equations 9 and 10; the ratios are used in Equation 11 to calculate the overall mixture viscosity where $S_{ij} = 1$ for nonpolar gases.

$$m_{ij} = \left[4M_iM_j/(M_i + M_j)^2\right]^{1/4} \tag{9}$$

$$A_{ij} = m_{ij}\left(\frac{M_j}{M_i}\right)^{1/2}\left[1 + \frac{\frac{M_i}{M_j} - \left(\frac{M_i}{M_j}\right)^{0.45}}{2\left(1 + \frac{M_i}{M_j}\right) + \frac{1 + \left(\frac{M_i}{M_j}\right)^{0.45}}{1 + m_{ij}}m_{ij}}\right] \tag{10}$$

$$\mu_{\text{mix}} = \sum_{i=1} \frac{x_i\sqrt{\mu_i}}{\frac{x_i}{\sqrt{\mu_i}} + \sum_{\substack{j=1 \\ j \neq i}} \frac{S_{ij}\,A_{ij}}{\sqrt{\mu_j}}x_j} \tag{11}$$

Lastly, the approach by Davidson estimates viscosity in terms of the fluidity of the gas mixture [9]. This method utilizes the momentum efficiency of the gas components to predict the mixture fluidity which is the reciprocal of the gas viscosity as given by Equations 12, 13, and 14 respectively. The empirical constant A was calculated as 0.375 using reported viscosities of 35 gas pairs [9].

$$E_{ij} = \frac{2\sqrt{M_i\,M_j}}{M_i + M_j} \tag{12}$$

$$f = \sum \frac{x_i\,x_j}{\sqrt{\mu_i\,\mu_j}}E_{ij}^A \tag{13}$$

$$\mu_{\text{mix}} = 1/f \tag{14}$$

3.2 Fluidization correlations

For a bed of particles, the minimum fluidization velocity U_{mf} is the gas velocity at which the drag force of the upward moving gas equals the weight of the particles. Kunii and Levenspiel [20] provide the following equation for calculating minimum fluidization velocity

$$U_{\text{mf}} = \frac{Re_{\text{p,mf}}\,\mu}{d_p\,\rho_g} \tag{15}$$

where μ is gas viscosity (kg/m·s), d_p is particle diameter (m), ρ_g is gas density (kg/m^3), and $Re_{p,mf}$ is the particle Reynolds number at minimum fluidization conditions. The Reynolds number is calculated using the Archimedes number (Ar) as follows

$$Re_{p,mf} = \left(a^2 + bAr\right)^{1/2} - a \tag{16}$$

$$Ar = \frac{d_p^3 \rho_g (\rho_s - \rho_g) g}{\mu^2} \tag{17}$$

where a and b are dimensionless constants which represent experimental coefficients. Some U_{mf} correlations in the literature are based on experimental data from Wen and Yu where a, b = 33.7, 0.0408; from Richardson where a, b = 25.7, 0.0365; and from Grace where a, b = 27.2, 0.0408 [20]. However, Kunii and Levenspiel [20] suggest the constants (a, b) can be derived from the Ergun pressure drop equation based on constants K_1 and K_2 where ϵ_{mf} is the bed void fraction at minimum fluidization and ϕ is sphericity of the bed particles. For this paper, U_{mf} is estimated based on the Ergun, Grace, Richardson, and Wen and Yu correlations.

$$a = \frac{K_2}{2K_1} \qquad b = \frac{1}{K_1} \tag{18}$$

$$K_1 = \frac{1.75}{\epsilon_{mf}^3 \phi} \qquad K_2 = \frac{150(1 - \epsilon_{mf})}{\epsilon_{mf}^3 \phi^2} \tag{19}$$

The terminal velocity U_t of a particle is the minimum gas velocity to entrain a particle of size d_p. This velocity can be estimated from the maximum velocity of a particle in free-fall through a fluid, which is given by Equation 20. Here, Re_p is the particle Reynolds number given by Equation 21 and C_D is the drag coefficient which was estimated from an emperical correlation developed by Haider and Levenspiel [15] and given by Equation 22.

$$U_t = \left[\frac{4d_p \left(\rho_s - \rho_g\right) g}{3\rho_g C_D} \right]^{1/2} \tag{20}$$

$$Re_p = \frac{d_p U_t \rho_g}{\mu_g} \tag{21}$$

$$C_D = \frac{24}{Re_p} \left[1 + \left(8.1716 e^{-4.0655\phi}\right) Re_p^{0.0964 + 0.5565\phi} \right] + \frac{73.69 Re_p e^{-5.0748\phi}}{Re_p + 5.378 e^{6.2122\phi}} \tag{22}$$

As shown in Equation 23, the convective heat transfer coefficient h in units of W/m^{2}K can be determined from the Nusselt number Nu where Re is the Reynolds number, d_p is the biomass particle diameter, d_b is the sand particle diameter, and k_g is the gas thermal conductivity. According to Collier et al.

[8], this approach is valid for $d_p < d_b$. The Reynolds number was determined from the gas density ρ (kg/m³), the minimum fluidization velocity U_{mf} (m/s), and the dynamic gas viscosity μ (kg/m·s) [29].

$$Nu = 2 + 0.9\, Re^{0.62} \left(\frac{d_p}{d_b} \right)^{0.2} = \frac{h\, d_p}{k_g} \qquad (23)$$

$$Re = \frac{\rho\, U_{mf}\, d_p}{\mu} \qquad (24)$$

3.3 Dimensionless numbers

As mentioned in the work of Pyle and Zaror [33], the rate of pyrolysis involves a balance between internal and external heat transfer due to heat transport and reaction. This balance is embodied by the dimensionless numbers Bi, Py^I, and Py^{II} which are determined from Equations 25, 26, and 27 respectively. The Biot number Bi represents the ratio of convective and conductive heat transport. The first pyrolysis number Py^I demonstrates the ratio of heat transfer by conduction to the rate of heat loss due to products leaving the particle. The second pyrolysis number Py^{II} is the effect of convective heat transfer to the external particle surface relative to the reaction heat loss. The Biot and pyrolysis numbers are calculated using the following parameters: h is the convective heat transfer coefficient (W/m²K), R is the radius or characteristic length of the biomass particle (m), k is the biomass thermal conductivity (W/m·K), ρ is the density of the biomass particle (kg/m³), K is the total rate constant in 1/s for the primary reactions, and C_p is the biomass heat capacity calculated from $103.1 + 3.867\,T$ where T is the biomass temperature in Kelvin.

$$Bi = \frac{h\, R}{k} \qquad (25)$$

$$Py^I = \frac{k}{\rho\, C_p\, R^2\, K} \qquad (26)$$

$$Py^{II} = \frac{h}{\rho\, C_p\, R\, K} \qquad (27)$$

The Prandtl number is a dimensionless number representing the ratio of momentum diffusivity to thermal diffusivity. It is calculated from the equation shown below where C_p is heat capacity (J/kg·K), μ is dynamic gas viscosity (kg/m·s), and k is thermal conductivity (W/m·K).

$$Pr = \frac{C_p\, \mu}{k} \qquad (28)$$

3.4 Biomass pyrolysis kinetics

A pyrolysis kinetics scheme based on the work of Di Blasi was implemented to predict the conversion of biomass into gas, tar, and char products [2, 3]. Fig-

ure 3 gives an overview of the scheme and its reaction mechanisms. Reactions 1–3 represent the primary conversion of biomass while reactions 4–5 are secondary reactions that reduce tar yield at long residence times. Reaction 6 is the conversion of moisture in the biomass to water vapor.
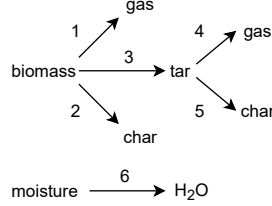

Figure 3: Diagram of the Di Blasi pyrolysis kinetics scheme for conversion of biomass to gas, tar, and char products.

The pyrolysis reactions were modeled as first-order Arrhenius type equations where the reaction rate is given as

$$r_i = C_i \, A_i \, e^{-E_i/RT} \tag{29}$$

where r_i is the rate of reaction i such that C_i is a mass based concentration, A_i is the pre-factor (1/s), E_i is the activation energy (kJ/mol), R is the gas constant, and T is the reaction temperature (K). Kinetic parameters for each reaction are listed in Table 1 where ΔH is the heat of reaction (kJ/kg). Based on the work performed by Lu et al.[21], the Di Blasi kinetics overpredict light gas production when using a coarse-grained DEM model. Consequently, we adjusted the pre-factor of reaction 4 by a factor of 0.2 which was determined by comparisons with NREL experiments.

Table 1: Kinetic parameters based on the Di Blasi biomass pyrolysis scheme where ΔH_{vap} is the heat of vaporization of water.

Reaction	A (1/s)	E (kJ/mol)	ΔH (kJ/kg)	Reference
1	4.38×10^9	152.7	-20	[3]
2	3.27×10^6	111.7	-20	[3]
3	1.08×10^{10}	148.0	255	[3]
4	8.56×10^5	108.0	-42	[2, 21]
5	1.00×10^6	108.0	-42	[2]
6	5.13×10^6	87.6	ΔH_{vap}	[7]

3.5 CFD-DEM simulation

A coarse-grained CFD-DEM model was implemented for biomass pyrolysis in MFiX, an open-source, Fortran-based code [34]. The coarse-grained CFD-DEM

model used in this work is an extension of the standard MFiX release. Gas phase transport was described using conservation equations of mass, momentum, energy, and chemical species in the Eulerian framework (Equations 30–33, respectively).

$$\frac{d(\epsilon_g \rho_g)}{dt} + \nabla(\epsilon_g \rho_g u_g) = S_\rho \tag{30}$$

$$\frac{d(\epsilon_g \rho_g u_g)}{dt} + \nabla(\epsilon_g \rho_g u_g u_g) = -\epsilon_g \nabla p + \nabla(\epsilon_g \tau) + \epsilon_g \rho_g g + S_u \tag{31}$$

$$\frac{d(\epsilon_g \rho_g E)}{dt} + \nabla(\epsilon_g \rho_g u_g E) = -\nabla Q + S_E \tag{32}$$

$$\frac{d(\epsilon_g \rho_g Y_i)}{dt} + \nabla(\epsilon_g \rho_g u_g Y_i) = -\nabla(D_i \nabla Y_i) + S_{Y_i} \tag{33}$$

where ϵ_g, ρ_g, u_g, p, τ, Q, and Y_i are gas phase volume fraction, density, velocity, pressure, stress tensor, conductive heat flux, and ith chemical species, respectively; while t is time, g is acceleration due to gravity, D_i is mass diffusion coefficient for species, S_ρ, S_u, S_E, and S_{Yi} are mass, momentum, energy, and chemical species source terms, respectively.

Fixed quantities of discrete particles with identical initial conditions were lumped into a computational coarse-grained parcel (CGP), whose motion was governed by Newton's second law of motion. All particle forces and contact dynamics were calculated on the parcel scale, whereas heat and mass transfers were calculated on particle scale and projected to the entire parcel. Accordingly, all particles in same coarse-grained parcel possess identical temperature, chemical species concentration, and momentum. The mass and diameter of each coarse-grained parcel is such that

$$m_{CGP} = m_p W \tag{34}$$

$$d_{CGP} = d_p W^{1/3} \tag{35}$$

where m_{CGP} is CGP mass, m_p is distinct particle mass, W parcel statistical weight, d_{CGP} is CGP diameter, and d_p is distinct particle diameter. Instantaneous accelerations (translational and rotational) for each coarse-grained parcel were calculated as

$$\frac{du_{CGP}}{dt} = g - \frac{F_p}{m_{CGP}} + \frac{F_c}{m_{CGP}} + \frac{F_d}{m_{CGP}} \tag{36}$$

$$\frac{d\omega_{CGP}}{dt} = \frac{T_{CGP}}{I_{CGP}} \tag{37}$$

where u_{CGP} and ω_{CGP} are the CGP translational and rotational velocities, g is acceleration due to gravity, m_{CGP} is CGP mass, T_{CGP} is net torque on the CGP, and I_{CGP} is CGP moment of inertia. The term F_p represents pressure gradient

force and was calculated as a product of the CGP volume and pressure gradient. The CGP collision forces F_C (parcel-parcel and parcel-wall collisions) were modeled according to the linear spring-dashpot model [27]. Since the number of CGP collisions is significantly lower than the number of collisions expected in a system with distinct particles, the CGP coefficient of restitution was modified as a correction for energy dissipations during collisions. The proposed modification to the CGP coefficient of restitution made use of the kinetic theory of granular flow [22] as

$$e_{CGP} = \sqrt{1 + (e_p^2 - 1)W^{1/3}} \tag{38}$$

where e_{CGP} is CGP coefficient of restitution and e_p is distinct particle coefficient of restitution.

Two different drag models were used to estimate CGP drag force F_d based on well-documented difference in the fluidization behavior of sand and biomass in the literature [28]. Drag force was estimated using the Ganser-corrected Gidaspow drag model for sand particles (bed material) and a filtered drag model for biomass particles. The Ganser correction [11] was coupled to the Gidaspow model [13] to account for non-sphericity of the sand particles as expressed below.

$$\beta_{Ganser} = \begin{cases} \beta_{Ergun} & \text{if } \epsilon_g \leq 0.8 \\ \beta_{WenYu} & \text{if } \epsilon_g > 0.8 \end{cases} \tag{39}$$

$$\beta_{Ergun} = 150 \frac{(1 - \epsilon_g)^2 \mu_g}{\epsilon_g d_{CGP}^2 \phi^2} + 1.75 \frac{(1 - \epsilon_g)\rho_g}{\epsilon_g d_{CGP}\phi} |u_g - u_{CGP}| \tag{40}$$

$$\beta_{WenYu} = \frac{3}{4} C_d \frac{(1 - \epsilon_g)\rho_g}{d_{CGP}\phi} |u_g - u_{CGP}| \epsilon_g^{-2.65} \tag{41}$$

$$C_d = \begin{cases} \frac{24}{ReK_1}(1 + 0.1118(ReK_1K_2)^{0.6567}) + \frac{0.4305K_2}{1 + \frac{3305}{ReK_1K_2}} & \text{if } Re < 1,000 \\ 0.44 & \text{if } Re \geq 1,000 \\ 0.0 & \text{if } Re = 0.0 \end{cases} \tag{42}$$

$$K_1 = \left(\frac{1}{3} + \frac{2}{3}\phi^{-0.5}\right)^{-1} - 2.25 \frac{d_{CGP}}{D} \tag{43}$$

$$K_2 = 10^{1.8148(-log\phi)^{0.5743}} \tag{44}$$

The filtered drag model (modified Sarkar drag model) used in this work for biomass particles was proposed by Gao et al. [12] and was found by the authors to have relatively high prediction strength across multiple flow regimes in fluidized bed. The modified Sarkar drag model was derived from a fine-grid simulation using the Wen-Yu drag model and can be computed as follows:

$$\beta_{Sarkar} = \beta_{WenYu}(1 - H_{Sakar}) \tag{45}$$

$$H_{Sakar} = \begin{cases} 0.95 \left(1 - e^{-\alpha_1 \alpha_2 (u_{\text{slip}}^* - u_0)^p}\right) & u_{\text{slip}}^* > u_0 \\ 0.0 & u_{\text{slip}}^* \leq u_0 \end{cases} \tag{46}$$

$$u_{\text{slip}}^* = \frac{|u_g - u_{CGP}|}{u_t} \tag{47}$$

$$\alpha_1 = \frac{\left(a_1 + a_2(1 - \epsilon_g) + a_3(1 - \epsilon_g)^2 + a_4(1 - \epsilon_g)^3 + a_5(1 - \epsilon_g)^4\right)}{1 + e^{100((1-\epsilon_g)-0.55)}} \tag{48}$$

$$\alpha_2 = \left(1 + \frac{a_6}{\Delta_{\text{filter}}^*} + \frac{a_7}{(\Delta_{\text{filter}}^*)^2}\right) \left(1 + \frac{a_8}{(u_{\text{slip}}^*)^2}\right) \tag{49}$$

$$u_0 = \frac{a_9 + a_{10}(1 - \epsilon_g)}{0.01 + (1 - \epsilon_g)^{a_{11}}} \left(1 + \frac{a_{12}}{\Delta_{\text{filter}}^*} + \frac{a_{13}}{(\Delta_{\text{filter}}^*)^2}\right) \tag{50}$$

$$p = \left(a_{14} + a_{15}(1 - \epsilon_g) + a_{16}(1 - \epsilon_g)^2\right) \left(1 + \frac{a_{17}}{\Delta_{\text{filter}}^*} + \frac{a_{18}}{(\Delta_{\text{filter}}^*)^2}\right) \tag{51}$$

$$\Delta_{\text{filter}}^* = max\left(\frac{g\Delta_{\text{filter}}}{u_t^2}, \frac{1}{2}\right) \tag{52}$$

$$\Delta_{\text{filter}} = 2(\Delta_x \times \Delta_y \times \Delta_z)^{1/3} \tag{53}$$

$$u_t = \frac{gd_{CGP}^2(\rho_{CGP} - \rho_g)}{18\mu_g} \tag{54}$$

$$\begin{array}{ccc} a_1 & a_2 & a_3 \\ a_4 & a_5 & a_6 \\ a_7 & a_8 & a_9 \\ a_{10} & a_{11} & a_{12} \\ a_{13} & a_{14} & a_{15} \\ a_{16} & a_{17} & a_{18} \end{array} = \begin{array}{ccc} 0.75597773 & 2.73931487 & -5.60196497 \\ -1.65853820 & 16.70299223 & -0.44145335 \\ 0.18195034 & -0.01827347 & 0.28441799 \\ -1.943573770 & 0.22177961 & 0.31175890 \\ -0.15971960 & 0.47750002 & 0.062794180 \\ 5.13011673 & 0.67680355 & -0.54535726 \end{array} \tag{55}$$

4 Model parameters

Particle size distribution of the biomass feedstock along with the mass flow rate associated with each size bin is given in Table 2. The initial biomass chemical composition used for the Di Blasi kinetics model is shown in Table 3. Other parameters related to the biomass and sand particles along with reactor operation and simulation settings are provided in Table 4. Biomass particle characteristics and properties are representative of loblolly pine while the bed particle characteristics are for a typical sand material. Operating conditions and reactor dimensions are based on the previously discussed NREL 2FBR fluidized bed pyrolysis unit.

Table 2: Particle size distribution for the biomass feedstock.

Sauter mean diameter (μm)	Mass fraction (%)	Mass flow rate (kg/hr)
278	12.1	0.018
344	51.0	0.076
426	34.2	0.051
543	2.7	0.004

Table 3: Initial chemical composition of the biomass feedstock for the Di Blasi kinetics model.

Species	Mass fraction (%)	Density (kg/m^3)
moisture	4.0	1,000
wood	95.9	500
ash	0.1	2,000
char	0.0	300

Table 4: Parameters for the biomass, sand (bed material), and reactor operation. Biomass C_p calculated from particle composition. Parameters for simulation settings also given.

Parameter	Value	Description
biomass particle		
e_p	0.2	particle-particle coefficient of restitution
e_w	0.2	particle-wall coefficient of restitution
e_s	0.2	particle-sand coefficient of restitution
μ_p	0.1	particle-particle coefficient of friction
μ_w	0.2	particle-wall coefficient of friction
μ_s	0.1	particle-sand coefficient of friction
k_n	100 N/m	particle spring constant
sand particle		
d_p	453 μm	particle diameter
ρ_p	2500 kg/m^3	particle density
C_p	830 J/(kg K)	particle heat capacity
ϕ	0.94	particle sphericity
e_p	0.61	particle-particle coefficient of restitution
e_w	0.61	particle-wall coefficient of restitution
μ_p	0.1	particle-particle coefficient of friction
μ_w	0.2	particle-wall coefficient of friction
k_n	100 N/m	particle spring constant
reactor operation		
d_{inner}	5.25 cm	inner reactor diameter
$H_{reactor}$	43.18 cm	reactor height
H_{static}	10.16 cm	static bed height
p_{gas}	101.325 kPa	gas pressure
T_{gas}	773.15 K	gas temperature
Q_{gas}	14 SLM	inlet gas flowrate
simulation settings		
$\Delta_x \times \Delta_y \times \Delta_z$	$4.3 \times 4.4 \times 4.3$ mm	CFD cell size
Δ_x	varies	time step
wt_{bio}	10	biomass parcel statistical weight
wt_{sand}	20	sand parcel statistical weight
s_{gas}	ideal	gas phase equation of state

Table 5 summarizes the CFD simulations conducted for this study. Each row represents a different simulation case that was performed for a particular gas composition. An additional 2.83×10^{-5} m^3/s of N_2 at 500°C was supplied at the fluidizing gas inlet and 2.55×10^{-5} m^3/s of N_2 at 25°C was supplied at the biomass feed inlet for all cases. For cases 1–8, the total flow rate was kept

constant, resulting in a constant superficial gas velocity inside the reactor. For cases 9–13, the gas flow rates were modified to maintain a constant $U/U_{mf} = 3$ in each simulation. Also, cases 9–13 represent H_2 mass fractions of 0.2, 0.4, 0.6, 0.8 and 1. Pure hydrogen is modeled because of its drastically different properties compared to the other gases (see following section); however, its applicability in experiments is limited due to safety concerns.

Table 5: CFD-DEM simulation cases for different gas mixtures. Columns denote gas flow rate in m^3/s at 500°C.

ID	Case	N_2	H_2	H_2O	CO	CO_2	CH_4
1	N_2	6.37e-04	0	0	0	0	0
2	H_2	0	6.37e-04	0	0	0	0
3	CO	0	0	0	6.37e-04	0	0
4	CO_2	0	0	0	0	6.37e-04	0
5	CH_4	0	0	0	0	0	6.37e-04
6	$0.5\ N_2 + 0.5\ CO$	3.18e-04	0	0	3.18e-04	0	0
7	$0.5\ N_2 + 0.5\ CO_2$	3.18e-04	0	0	0	3.18e-04	0
8	$0.22\ N_2 + 0.78\ H_2$	1.42e-04	4.95e-04	0	0	0	0
9	$0.10\ N_2 + 0.90\ H_2$	6.17e-05	5.75e-04	0	0	0	0
10	$0.05\ N_2 + 0.95\ H_2$	2.89e-05	6.08e-04	0	0	0	0
11	$0.02\ N_2 + 0.98\ H_2$	1.12e-05	6.26e-04	0	0	0	0
12	H_2	0	6.37e-04	0	0	0	0

5   Results and discussion

This section provides results and related discussions for modeling the effects of different fluidization gases on the operation of a bubbling fluidized bed reactor. Gas effects on the pyrolysis yields of the biomass feedstock are also presented and discussed.

5.1   Pure gas properties

Molecular weight, viscosity, density, thermal conductivity, heat capacity, and the Prandtl number of the individual gases investigated in this paper are shown in Figure 4. The gas properties were calculated at a pressure of 101,325 Pa and a temperature of 773.15 K (500°C). The lightest gas in terms of molecular weight and density is hydrogen while the heaviest gas is carbon dioxide. The highest viscosity is noted for the nitrogen gas while hydrogen has the lowest viscosity. The largest thermal conductivity is for hydrogen at approximately 0.36 W/(m K) while the other gases remain below 0.12 W/(m K). The highest heat capacity is obtained for methane at 62 J/(mol K) while the lowest is for hydrogen at 29 J/(mol K). The Prandtl number is similar for all the gases except for water vapor.
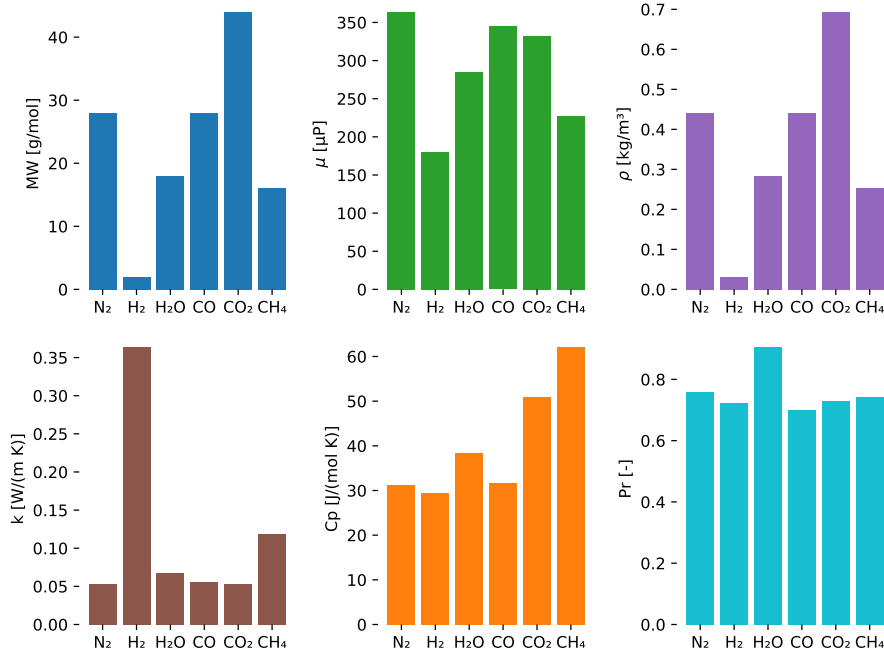
Figure 4: Comparison of molecular weight (MW), viscosity (μ), density (ρ), thermal conductivity (k), heat capacity (Cp), and Prandtl number (Pr) for each gas at 101,325 Pa and 773.15 K (500°C).

5.2 Gas mixture properties

Comparisons of the calculated viscosity of a H_2/N_2 gas mixture to measured values obtained from literature are shown in Figure 5. The models by Herning and Zipperer as well as Brokaw match well with the experimental data for a range of mixture ratios. This is contradictory to the Davidson report which does not recommend the Herning and Zipperer model for hydrogen mixtures [9]. The Davidson and Graham models significantly underpredict the mixture viscosity while the Wilke model tends to overestimate the viscosity. Similar results are obtained for a H_2/O_2 gas mixture as shown in Figure 6.
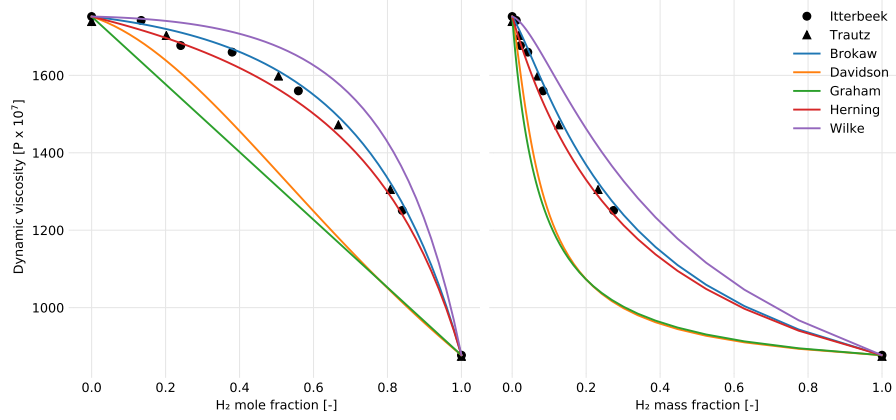
Figure 5: Viscosity of a H_2/N_2 mixture at 291.1 K (18°C). Calculated values represented by line profiles. Experiment data points from [18, 35] shown as symbols.
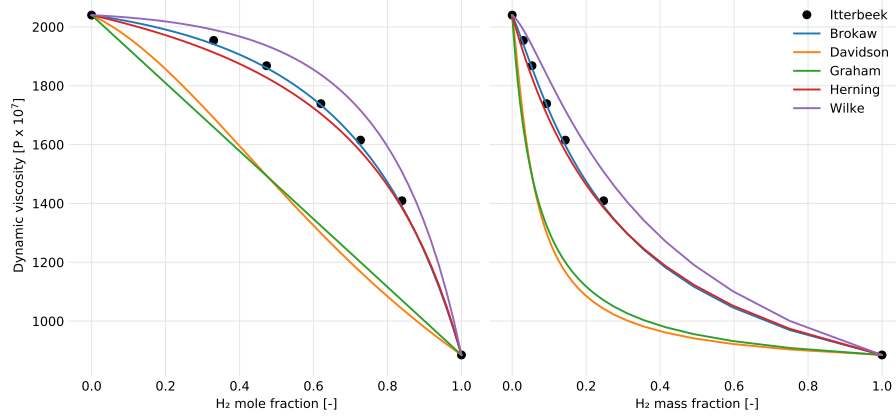
Figure 6: Viscosity of a H_2/O_2 mixture at 293.6 K (20°C). Calculated values represented by line profiles. Experiment data points from [18] shown as symbols.

Properties for molecular weight, viscosity, and density for the gas mixtures investigated in this paper are shown in Figure 7. Similar to the individual gas properties, the mixture properties were calculated at 101,325 Pa and 773.15 K (500°C). The viscosity of the gas mixture was determined using the Herning and Zipperer method (Equation 6). The mole fraction of each gas in the mixture is given by the values shown at the top of each column in the figure. For example, the nitrogen and hydrogen mixture is comprised of 22% nitrogen and 78% hydrogen which is labeled as $0.22 + 0.78$. As expected, the carbon dioxide

mixture is the heaviest in terms of molecular weight and density while the nitrogen and hydrogen mixture is the lightest. The most viscous mixture is the nitrogen and carbon monoxide where as the hydrogen mixtures are the least viscous.
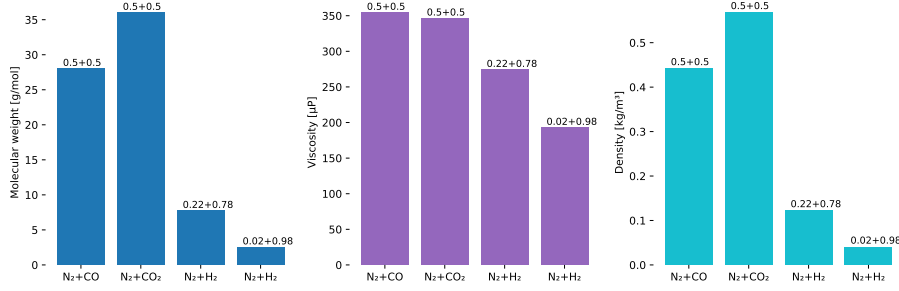

Figure 7: Comparison of gas mixture properties for molecular weight, viscosity, and density at 101,325 Pa and 773.15 K. Mole fraction of each gas component is shown at the top of each column.

5.3 Fluidization characteristics

Minimum fluidization velocity (U_{mf}) of the bed material for the different fluidization gases is presented in Table 6. Hydrogen requires about twice the gas velocity to fluidize the bed of sand compared to the nitrogen, carbon monoxide, and carbon dioxide gases. This is due to hydrogen's lower viscosity and much lower density compared to the other gases. Water vapor and methane require moderately higher fluidization velocities compared to the nitrogen gas. A comparison of U_{mf} for the various fluidization gases is displayed in Figure 8.

Table 6: Minimum fluidization velocity (m/s) of the bed material calculated from various correlations for different fluidization gases. Last row represents the average U_{mf} value for each gas.

U_{mf}	N_2	H_2	H_2O	CO	CO_2	CH_4
Ergun	0.14	0.30	0.18	0.15	0.16	0.23
Grace	0.10	0.21	0.13	0.11	0.11	0.16
Richardson	0.10	0.20	0.12	0.10	0.11	0.15
Wen and Yu	0.08	0.17	0.11	0.09	0.09	0.13
average	0.11	0.22	0.14	0.11	0.12	0.17

The superficial gas velocity (U_s) of the nitrogen gas flow is calculated as 0.3072 m/s which is based on the 14 SLM gas flow through the distributor plate. Using this value, the ratio of U_s to U_{mf} is shown in Table 7 for different fluidization gases. The BFB pyrolysis reactor at NREL typically operates at

a U_s/U_{mf} of 3 with nitrogen gas. For gases such as H_2, H_2O, CO, CO_2, and CH_4, the gas flow into the reactor must be increased to have similar fluidized bed characteristics as the nitrogen case. A comparison of the increased U_s for each gas along with the associated U_s/U_{mf} is shown in Figure 9. As expected, the hydrogen gas flow must be approximately doubled compared to the nitrogen case to achieve similar fluidization of the bed material.

Table 7: Ratio of U_s to U_{mf} for different fluidization gases. Last row represents the average U_s/U_{mf} value for each gas.

U_s/U_{mf}	N_2	H_2	H_2O	CO	CO_2	CH_4
Ergun	2.13	1.04	1.67	2.02	1.97	1.34
Grace	2.99	1.47	2.35	2.84	2.76	1.88
Richardson	3.16	1.55	2.48	3.00	2.91	1.98
Wen and Yu	3.69	1.82	2.90	3.50	3.39	2.32
average	2.99	1.47	2.35	2.84	2.76	1.88
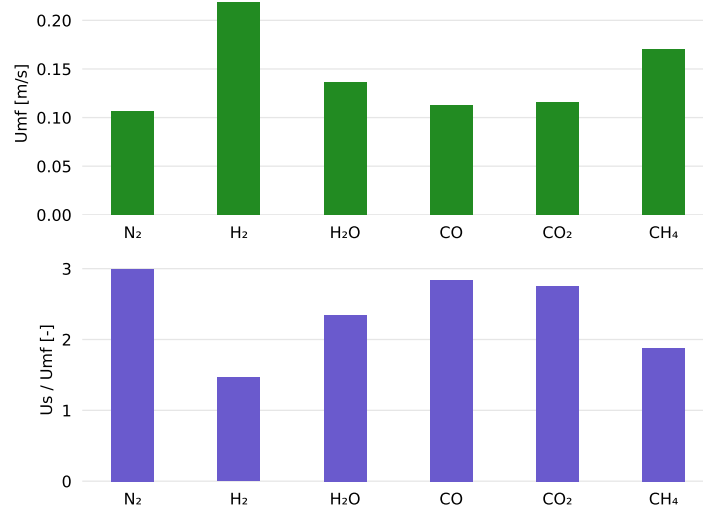
Figure 8: Comparison of the minimum fluidization velocity (U_{mf}) and the ratio of U_s/U_{mf} for different fluidization gases. Superficial gas velocity is U_s.
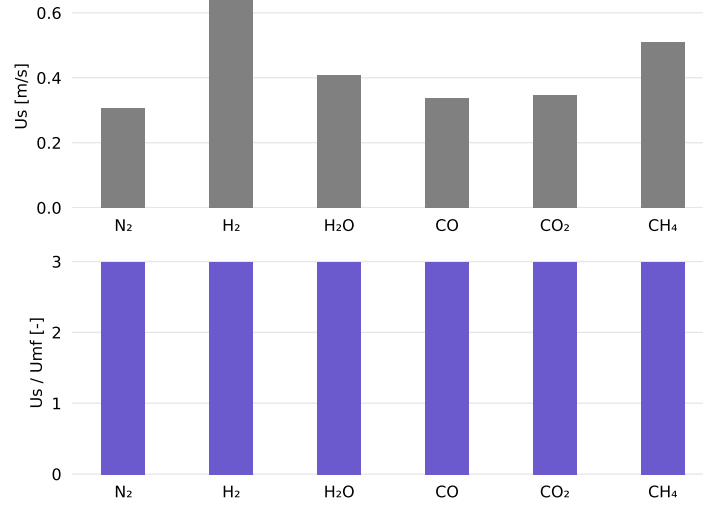
Figure 9: Comparison of the superficial gas velocity (U_s) and the associated U_s/U_{mf} for different fluidization gases. Minimum fluidization velocity is U_{mf}.

The Reynolds number was calculated using an average biomass particle diameter of 369.4 μm and the mean U_{mf} value. Next, the Nusselt number along with the associated convective heat transfer coefficient were calculated for each carrier gas as shown in Table 8 and Figure 10. The highest heat transfer coefficient is estimated for H_2 while the second highest result is for CH_4. This is largely due to the higher thermal conductivity of the hydrogen and methane compared to the other gases. Due to the higher heat transfer rate to the biomass particle in the hydrogen environment, one can expect the biomass to pyrolyze more quickly with the hydrogen carrier gas.

Table 8: Comparison of the Reynolds number, Nusselt number, and convective heat transfer coefficient (h) for different fluidization gases.

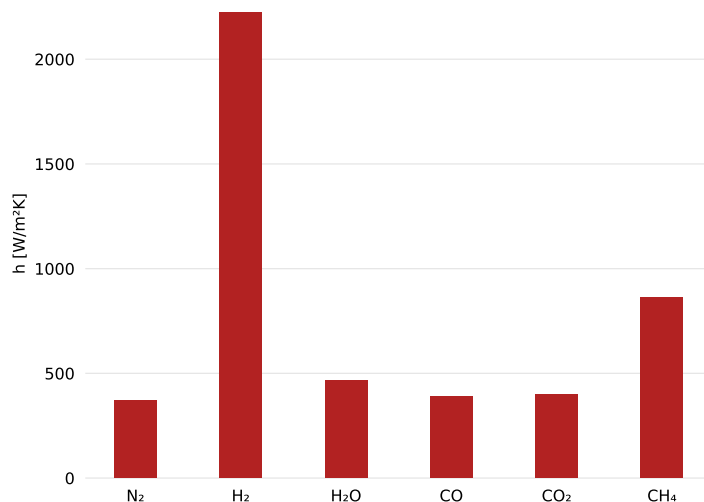| Gas	U_{mf}	Re	Nu	h
N_2	0.11	0.48	2.55	369.45
H_2	0.22	0.14	2.26	2224.25
H_2O	0.14	0.50	2.56	464.54
CO	0.11	0.53	2.58	389.53
CO_2	0.12	0.89	2.81	399.83
CH_4	0.17	0.70	2.69	862.61

Figure 10: Convective heat transfer coefficient (h) for different fluidization gases. Values based on average biomass particle size and average minimum fluidization velocity.

5.4 Evaluation of the kinetic scheme

The Di Blasi kinetics were put to use in a batch reactor model to investigate the time scales associated with the reaction mechanisms. Figure 11 is an overview of the biomass conversion and pyrolysis yields using the Di Blasi kinetics in a batch reactor at 773.15 K (500°C). At this temperature, without the effects of secondary reactions, the kinetics offer a maximum achievable tar yield of 78% within 5 seconds. However, if secondary reactions occur during the entire pyrolysis process then a maximum tar yield of only 53% is possible. Modifying reaction 4 by a factor of 0.2, decreases the gas yield while increasing tar and char yields. The Di Blasi kinetics suggest that minimizing the extent of secondary reactions is critical to producing the maximum possible tar yield.

A range of reaction temperatures were applied to the Di Blasi kinetics in the batch reactor model as shown in Figure 12. The kinetics suggest that temperature can increase the rate of primary tar production while decreasing devolatilization time. When secondary reactions occur during the entire pyrolysis process, maximum tar yields are realized at higher temperatures but with shorter residence times. These results suggest that if secondary reactions are minimized then maximum tar yield can be achieved given an appropriate residence time.
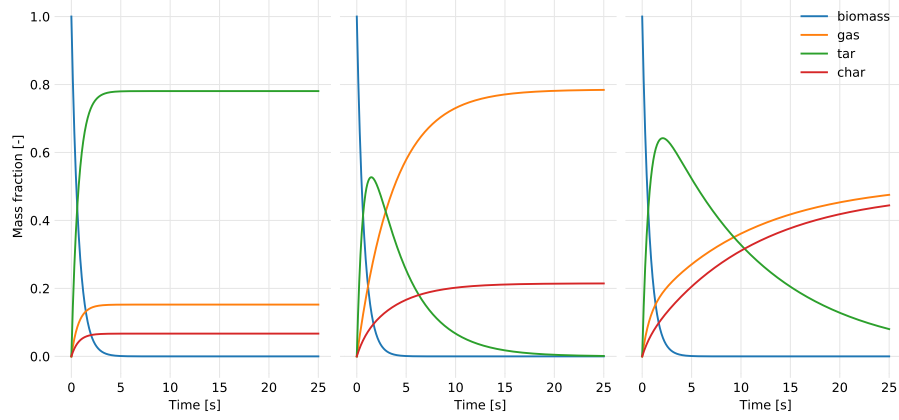
Figure 11: Biomass conversion and product yields in a batch reactor model at 773.15 K (500°C) according to the Di Blasi kinetic reactions. Primary reactions only (left). Primary and secondary reactions (center). Primary and secondary reactions using modified reaction 4 (right).
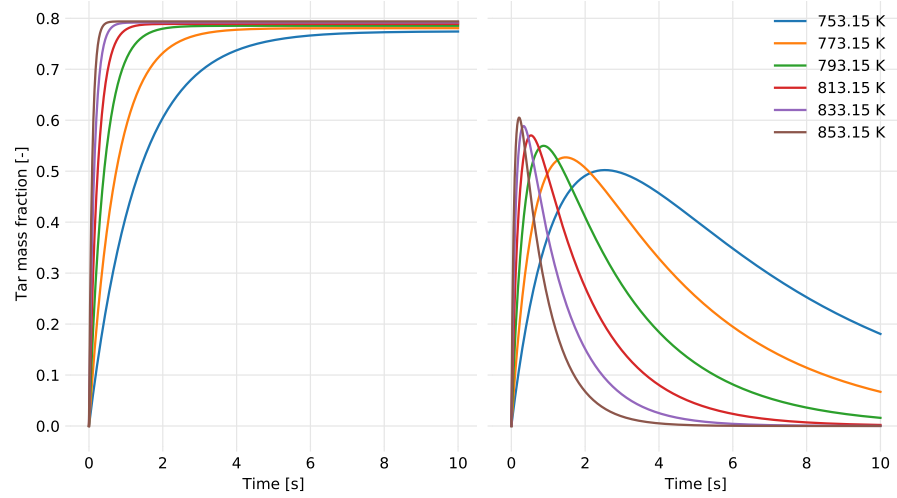

Figure 12: Tar yields for reaction temperatures of 753.15–853.15 K (480–580°C) using the Di Blasi kinetics in a batch reactor model. Results shown for primary tar (left) along with primary and secondary tar (right).

5.5 Limiting factors for biomass pyrolysis

Gas influence on the pyrolysis limiting regimes is shown in Figure 13 for a biomass particle diameter of 369.4 μm. The regime map suggests that gas

properties have little effect on the limiting mode of pyrolysis. However, when comparing a range of particle diameters, the differences are more pronounced as seen in Figure 14. For larger particles, conduction becomes the limiting mode of pyrolysis especially for the hydrogen gas. For smaller particles, nitrogen gas promotes isothermal conditions along with a kinetically limited regime.
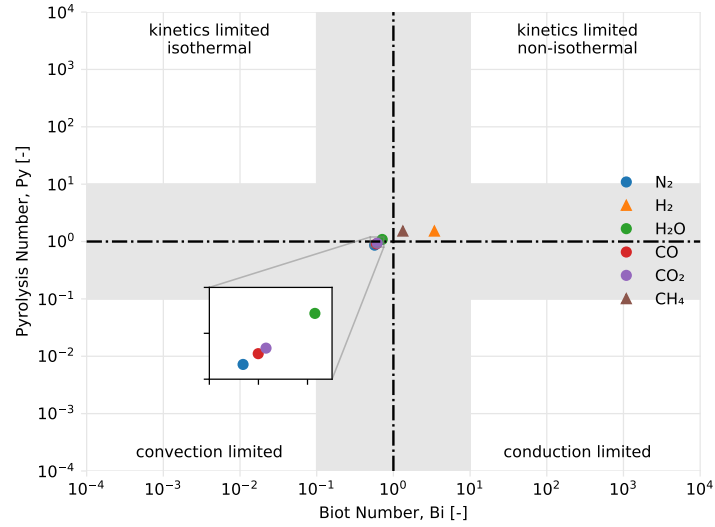

Figure 13: Comparison of carrier gas effects on pyrolysis regime for a 369.4 μm biomass particle. Grey region means no dominant mechanism controlling pyrolysis.
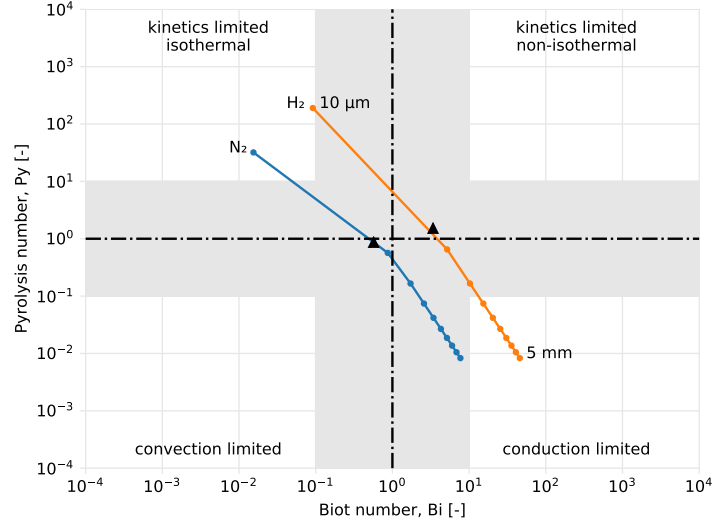
Figure 14: Comparison of nitrogen and hydrogen gas effects for biomass particles ranging from $10 \mu m$ to 5 mm in diameter. Triangle markers symbolize 369.4 μm biomass particle diameter. Grey region means no dominant mechanism controlling pyrolysis.

5.6 CFD-DEM validation

The predicted yield of pyrolysis products (bio-oil, light gases, and biochar) was validated against experimental data of biomass pyrolysis using the same NREL 2FBR reactor system that was modeled and simulated in this work [XXX]. The process variables used in the experimental work are consistent with those implemented for the N_2 and H_2 cases (run ID = 1 and 2, respectively). Table 9 shows that the predicted yields of pyrolysis products closely follow the experimental data. The magnitude of the relative prediction deviation ranged between 5.7% and 14.9%. The CFD–DEM simulation seems to generally overestimate the yield of pyrolysis products, except in the case of the light gas yield for the H_2 case (run ID = 2). This skewness in the product yield predictions relative to experimental data is attributable to mass closure issues in the experimental data. The mass closure for the experimental data was about 94%. A mass-proportional adjustment of the experimental data to enforce 100% mass closure decreases the average prediction deviation by about a factor of 2.

23

Table 9: CFD–DEM model validation against experimental data. Product yields were calculated on a biomass weight basis.

Run ID	Fluidizing gas	Pyrolysis product	Pyrolysis yield (wt.%)		Relative deviation (%)
			Experiment	Simulation	
1	N_2	bio-oil	70.2	74.3	5.8
1	N_2	light gas	11.6	12.5	7.7
1	N_2	biochar	12.5	13.2	5.7
2	H_2	bio-oil	68.8	74.8	8.8
2	H_2	light gas	14.0	13.1	-6.0
2	H_2	biochar	10.5	12.1	14.9

When the fluidizing gas was changed from N_2 to H_2, the developed CFD–DEM model was able to qualitatively predict the increase in the yield of light gases and decrease in the yield of biochar yield in consonance with the experimental data. The predicted bio-oil yield slightly increased when fluidizing gas was changed from N_2 to H_2, contrary to experimental data showing a decrease. The relative change in bio-oil yield between N_2 to H_2 was however nominal for both experimental data (2%) and CFD–DEM prediction (1%).

5.7 Fluidizing gas effect on pyrolysis performance at a constant flow rate

The yields of pyrolysis bio-oil, light gas, and biochar for the different fluidizing gases at a constant flow rate are compared in Figure 15. The observed differences in the pyrolysis product distribution among the fluidizing gases were minimal. The highest bio-oil yield of 75.1 wt.% and lowest bio-oil yield of 73.5 wt.% were obtained when pure CH_4 and CO were used as fluidizing gas, respectively. The bio-oil yield was slightly higher when any of H_2, CH_4, and CO replaced N_2 as the fluidizing gas. The evidence reviewed here suggests that light gas may be recirculated at a constant flow rate during pyrolysis without causing substantial losses in bio-oil yield.
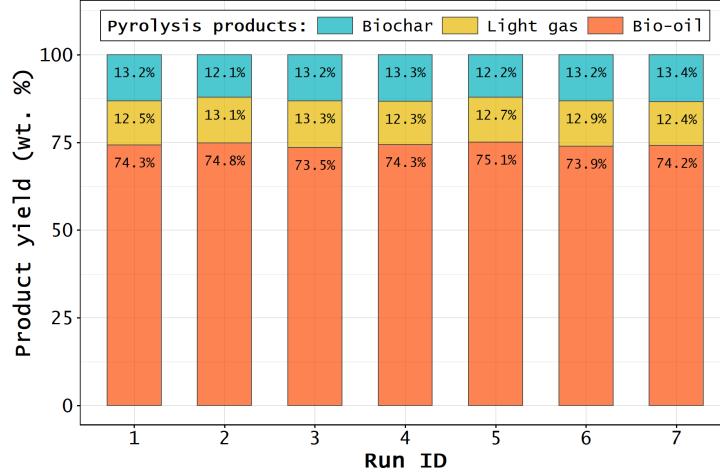
Figure 15: Pyrolysis product distributions for different fluidizing gas at a constant flow rate. Product yields were calculated on a biomass weight basis. Run ID 1, 2, 3, 4, 5, 6, and 7 represent fluidizing gas N_2, H_2, CO, CO_2, CH_4, N_2/CO, and N_2/CO_2 respectively.

A summary of the particle residence time for each fluidizing gas considered is given in Table 10. It was unsurprising to find that the median particle residence time increased with increasing initial diameter of the biomass particles. The difference in particle residence time among the fluidizing gases also increased with increasing initial diameter of biomass particles. In other words, the impact of fluidizing gas on particle residence time is stronger for larger particles and weaker for smaller particles.

Table 10: Particle residence time of biomass particle for different fluidizing gas at a constant flow rate and different initial particle diameter where d_p is initial biomass particle diameter.

Run ID	Fluidizing gas	Median particle residence time (s)			
		$d_p = 278\ \mu m$	$d_p = 344\ \mu m$	$d_p = 426\ \mu m$	$d_p = 543\ \mu m$
1	N_2	5.9	7.3	8.8	10.9
2	H_2	7.9	13.6	34.3	77.4
3	CO	6.8	8.1	9.7	12.2
4	CO_2	6.5	7.7	9.1	10.5
5	CH_4	6.5	8.7	12.6	21.8
6	N_2/CO	6.6	8.0	9.5	11.4
7	N_2/CO_2	6.4	7.7	8.9	10.8

Figure 16 shows the gas phase temperature, void volume fraction, and bio-oil degradation rates profile along the reactor height for different fluidizing gas at

a constant flow rate. The gas-phase temperature was higher in the freeboard than in the bed. This is attributed to the fact that enthalpy for biomass pyrolysis reactions is drawn from inside the bed because pyrolysis reactions occur predominantly inside the bed. Additionally, the gas temperature was relatively unchanged along the reactor height within the bed whereas, in the freeboard, the gas temperature increased towards the reactor outlet. Also noteworthy is the fact that the gas temperature along the reactor height was consistently highest when H_2 was used as fluidizing gas (Figure 16a). This observation is attributable to the large difference in the thermal conductivity of H_2 compared to the other fluidization gases (Figure 4). The average height of the fluidized bed was about 0.14 m for all the fluidizing gases considered, except for H_2 which produced a lower bed height (Figure 16b). The bed height was determined as the position along the reactor height where the void volume fraction approached 0.7.
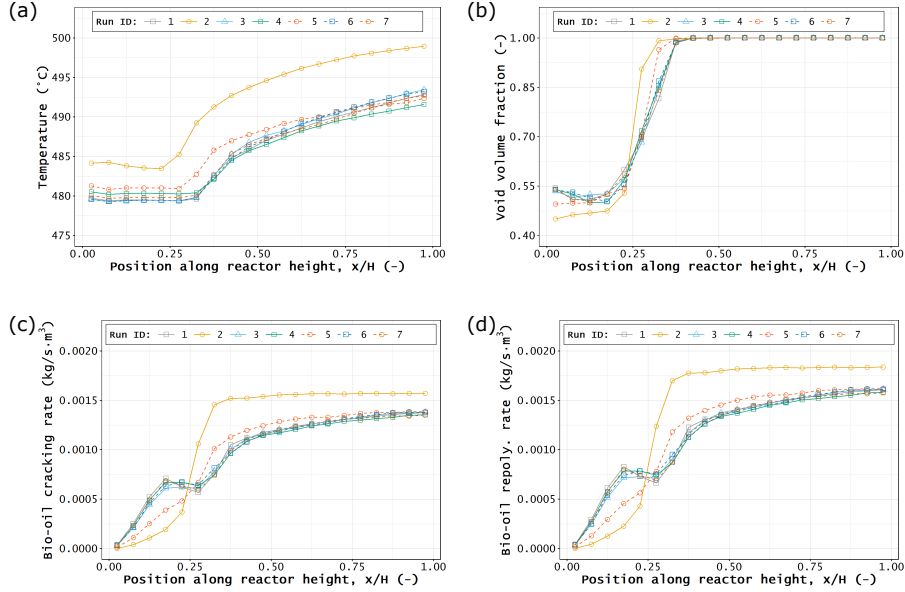

Figure 16: Profile of (a) fluid temperature, (b) fluid volume fraction, (c) bio-oil cracking reaction rate, (d) bio-oil repolymerization reaction rate along the reactor height for different fluidizing gas at a constant flow rate. The reactor height (0.43 m) is denoted by the letter H. Run ID 1, 2, 3, 4, 5, 6, and 7 represent fluidizing gas N_2, H_2, CO, CO_2, CH_4, N_2/CO, and N_2/CO_2 respectively.

The observed degradation rates for both the particle and vapor phases were substantially affected by the fluidizing gas used. The shape of the bio-oil cracking rate profile along the reactor height was similar to that of the bio-oil repolymerization rate for all the fluidizing gases considered (Figure 16c and Figure 16d). Bio-oil degradation rates were higher in the freeboard than in the bed.

The overall bio-oil degradation rates with H_2 as the fluidizing gas were substantially higher than those observed with other fluidizing gases. The reactor volume-averaged bio-oil cracking and repolymerization rates were 1.17×10^{-3} and 1.37×10^{-3} kg/s·m^3 for H_2, respectively 9.92×10^{-4} and 1.16×10^{-3} kg/s·m^3 for N_2, respectively. This data demonstrates that bio-oil degradation rates were 18% higher when H_2 replaced N_2 as the fluidizing gas. This observation explains the reason why despite H_2 yielding the highest particle heating and mass-loss rates (Figure 17), and one of the longest residence times (Table 10), its bio-oil yield is marginally different from the bio-oil yield with other fluidizing gases, especially N_2. When H_2 was used as fluidizing gas, biomass particles experienced significantly higher heating rates, and consequently higher mass-loss rates, compared to when other fluidizing gases were used. The impact of fluidizing gas on the heating and mass-loss rates was higher for larger particles. Generally, biomass heating and mass-loss rates follow the order: $H_2 > CH_4 > CO > N_2 > N_2/CO > N_2/CO_2 > CO_2$ which correlates well with the effective thermal conductivity of the fluidizing gas.
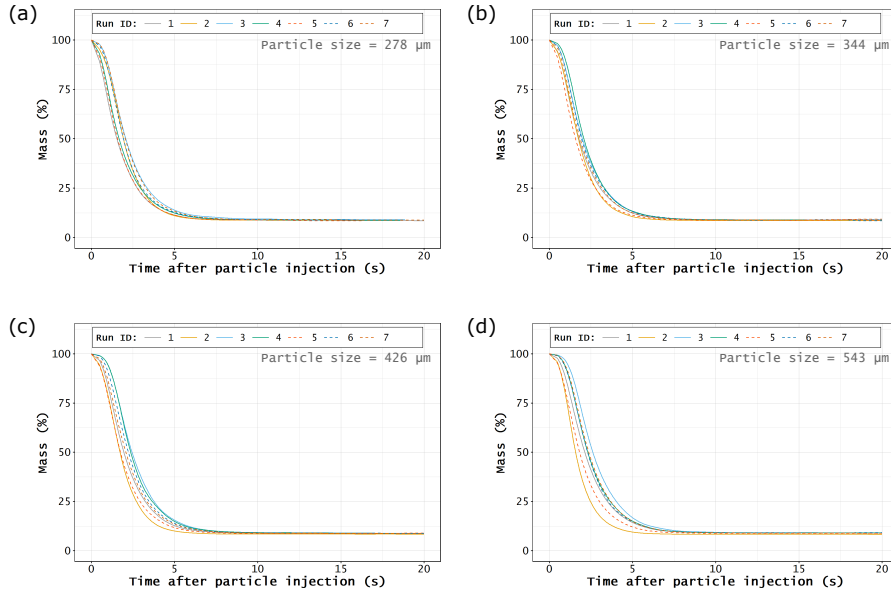

Figure 17: Average biomass particle thermogravimetry curve for different fluidizing gas at a constant flow rate (a) particle size = 278 μm, (b) particle size = 344 μm, (c) particle size = 426 μm, and (d) particle size = 543 μm. Run ID 1, 2, 3, 4, 5, 6, and 7 represent fluidizing gas N_2, H_2, CO, CO_2, CH_4, N_2/CO, and N_2/CO_2 respectively.

Overall, our findings indicate that light gas produced during pyrolysis can be recirculated as fluidizing gas at a constant flow rate without detrimental consequences on pyrolysis performance. Additionally, we demonstrated that

27

fluidizing gas can notably increase biomass heating and mass-loss rates (pyrolysis conversion rate). This suggests potential process intensification implications because heating and mass-loss rates represent a major bottleneck in conventional pyrolysis systems. Achieving increased heating and mass-loss rates may lead to significant improvement in process throughput and scaleup.

5.8 Fluidizing gas effect on pyrolysis performance with constant U_s/U_{mf}

As discussed in Section 5.3, the value of U_s/U_{mf} varies for each fluidizing gas composition when the flowrate is kept constant. As a result, the dynamic behavior of the bed, which U_s/U_{mf} characterizes, varies with the gas composition. These differences are most pronounced between N_2 and H_2 which have U_s/U_{mf} values of 3.0 and 1.5, respectively, when U_s remains constant. To investigate the effect of gas properties on pyrolysis yields, the mass fraction of H_2 was varied between 0 and 1 (with the N_2 as the remaining fraction) while maintaining a constant $U_s/U_{mf} = 2.99$. Figure 18 shows the average particle temperature and mass as a function of time after injection into the reactor for each particle size in both N_2 and H_2 fluiding gas streams. Here it can be seen, as for the constant U_s case, the larger heat transfer coefficient associated with the H_2 fluidizing gas ($h_{H2} = 2224.3$, $h_{N2} = 368.5$ W/m^{2}K) result in greater rates of heat transfer and mass loss. Additionally, the nearly identical time distributions of the particle temperature and mass for H_2 with constant U_s and U_s/U_{mf} indicates that total heat transfer to a particle in bubbling fluidized bed is independent of the gas velocity. This is consistent with previous results that while convection increases with gas velocity, this increase is offset by decreases in conduction between solids in the bed [8, 42].
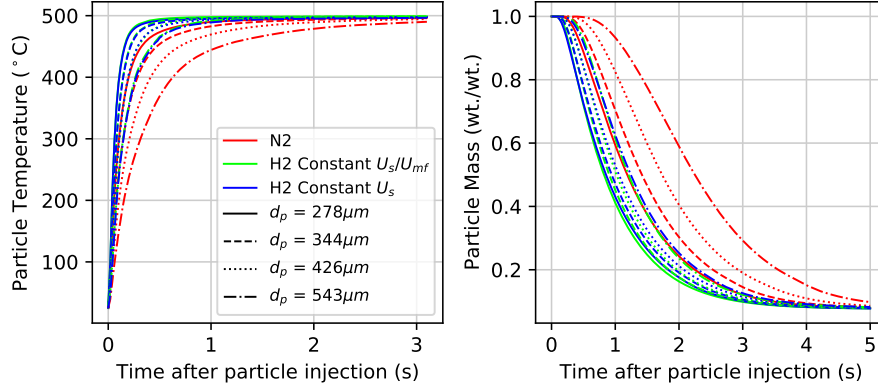

Figure 18: Average particle temperature (left) and density (right) as a function of residence time in reactor for N_2 and H_2 carrier gasses. For H_2 carrier gas, results with both constant U_s and U_s/U_{mf} are provided.

At the reactor conditions and particle sizes investigated, the gas velocities are insufficient for biomass particles to elutriate from the reactor at their initial density. Therefore, the particle remains in the reactor until its density is sufficiently reduced from pyrolysis. This can be seen in Figure 19, which contains the normalized terminal velocities, U_t/U_s, of each biomass particle size for N_2 and H_2 (both constant U_s and U_s/U_{mf}) fluidizing gases as a function of particle density. For the N_2 fluidizing gas, the maximum densities at which $U_s > U_t$ are approximately 300, 200, 140 and 90 kg/m^3 for particle sizes of 278, 344, 426 and 543 μm, respectively. These maximum densities decrease to 150, 100, 65 and 40 kg/m^3 for H_2 at the same gas velocities, but are similar when the flows are increased to maintain a constant U_s/U_{mf}. This suggests the residence time of the particles is a function of both the terminal velocity of the particles for the given gas mixture, and the rate of heat transfer to the particles, which defines the rate of mass loss from pyrolysis. The result of this can be seen in Figure 20, which contains the average residence time for each particle diameter plotted against the H_2 mass fraction in the fluidizing gas. For increasing x_{H2} and constant U_s/U_{mf}, the increasing heat transfer rates result in particles reaching densities necessary for elutriation faster. This, coupled with a nearly constant U_t/U_s, results in the average particle residence time decreasing as H_2 x_{H2} increases, with the average for all biomass particles decreasing from 5.23s at $x_{H2} = 0$ to 4.64s at $x_{H2} = 1$. For constant U_s, the increased heat transfer rate of H_2 are offset by the higher normalized terminal velocity, resulting in the average particle residence time decreasing only 2.4% compared to those of the N_2 fluidizing gas.
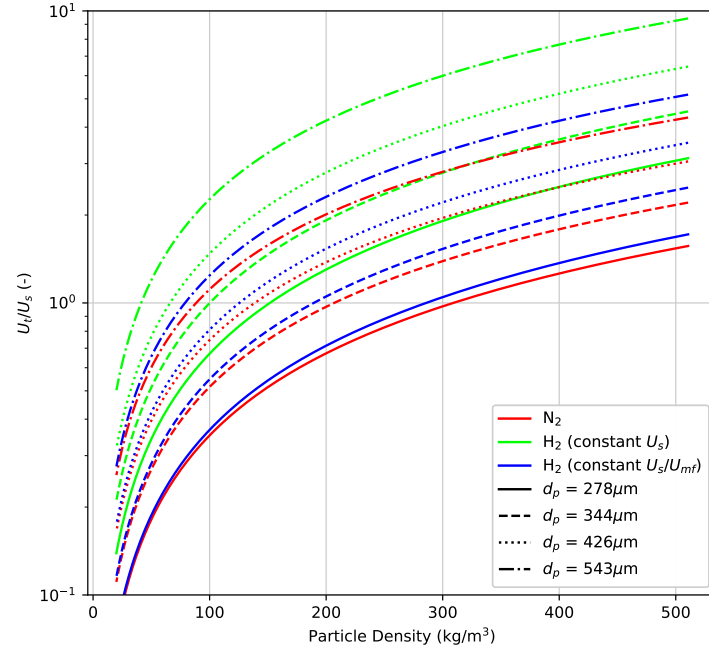
Figure 19: Terminal velocity of each biomass particle size normalized by superficial gas velocity as a function of particle density for N_2 and H_2 carrier gasses. For H_2 carrier gas, results with both constant U_s and U_s/U_{mf} are provided.
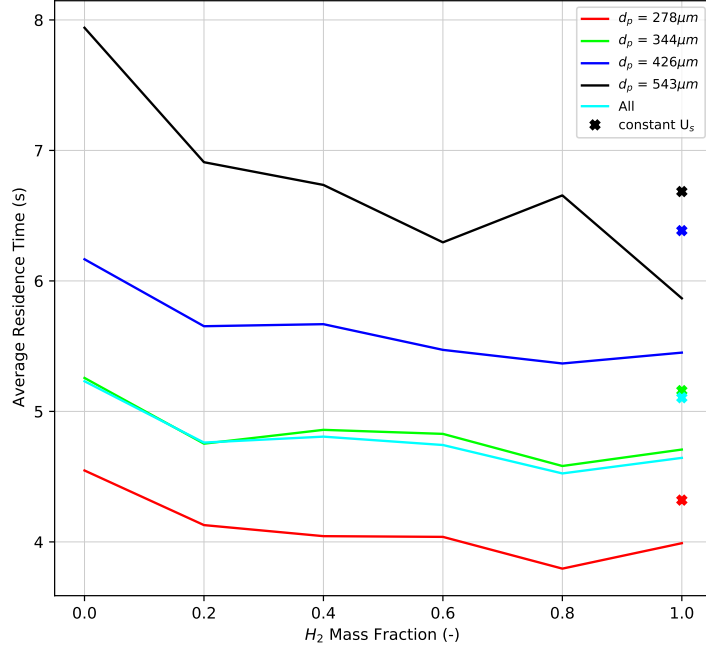
Figure 20: Average particle residence time as a function of H_2 mass fraction in fluidizing gas at constant U_s/U_{mf}. Average residence times for H_2 fluidizing gas with constant U_s indicated by markers in the plot.

The effect of maintaining a constant U_s/U_{mf} while increasing the mass fraction of H_2 in the fluidizing gas is shown in Figure 21, which contains plots of the product yields as well as the fraction of biomass converted for each gas composition and particle size. For $d_p >= 344$ μm, the fraction of biomass converted remains nearly constant for each H_2 mass fraction, while for 278 μm, the fraction decreased slightly, a result of the increased gas velocities. For all particle sizes, the yields of light gasses and char decreased with increasing H_2 mass fraction with averages decreasing from 12.8% to 8.38% and 11.1% to 9.67%, respectively. These decreases in the char and light gas yields are accompanied by increases in the bio-oil yields, with the average increasing from 74.3% in N_2 to 79.5% in H_2. For 278 μm diameter particles, the bio-oil yield initially increased with H_2 mass fraction before leveling off between $x_{H2} = 0.8$ and 1.0, which resulted from the decreasing fraction of biomass being pyrolyzed before exiting the reactor. The increased yields in bio-oil for increased H_2 mass fractions results from the low density of H_2 allowing for higher gas velocities while maintaining similar particle residence times. The similar residence times ensure the most of the biomass is converted to its pyrolysis products. With the higher gas velocities, the oil being produced is removed faster, reducing the amount lost to secondary reactions converting it to char (repolymerization) and light gas (cracking). This can be

seen in Figure 22 which shows the time and volume averaged cracking and re-polymerization reaction rates in the reactor for each H_2 mass fraction. While maintaining a constant gas velocity when switching the fluidizing gas from N_2 to H_2 results in a slight increase in both secondary reactions, increasing the gas flowrate to maintain a constant U_s/U_{mf} leads to decreases of 35.8% and 71.3% for the polymerization and cracking reaction rates, respectively. This leads to the increased bio-oil production and subsequent decrease in light gas and char production when using H_2 as the fluidizing gas.
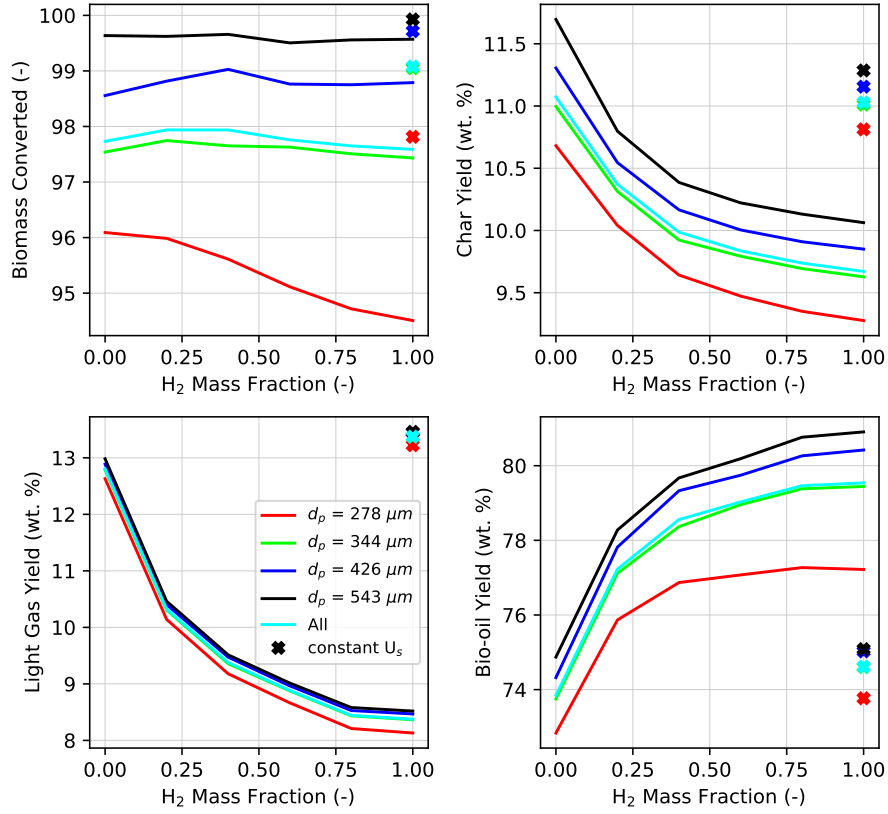

Figure 21: Fraction of biomass converted and product yields as a function of H_2 mass fraction at constant U_s/U_{mf}. Biomass converted and product yields for H_2 fluidizing gas with constant U_s indicated by markers in the plot.
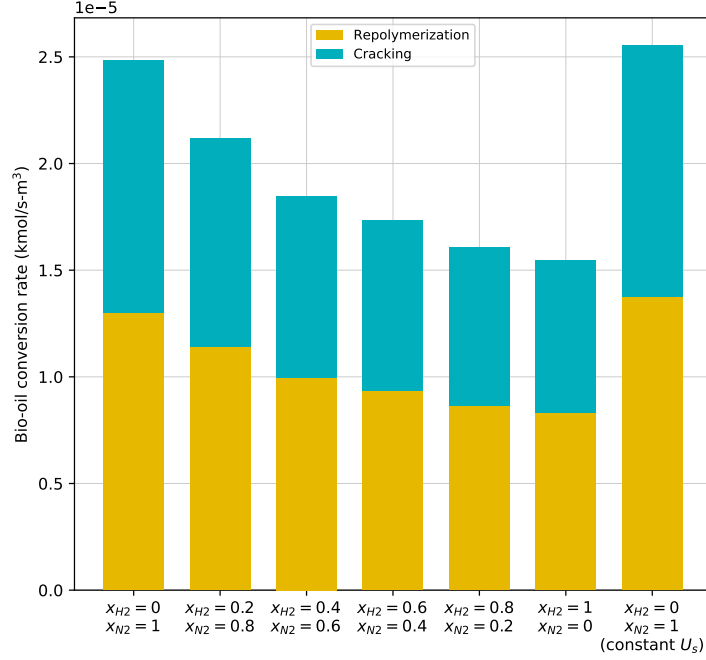
Figure 22: Volume and time averaged secondary reaction rates as a function of H_2 mass fraction at constant U_s/U_{mf}. Reaction rates with H_2 fluidizing gas and constant U_s included for comparison.

6   Conclusion

Gas effects in a fluidized bed biomass pyrolysis reactor using engineering correlations, low-order models, and CFD simulations were investigated for N_2, H_2, H_2O, CO, CO_2, and CH_4 carrier gas mixtures. Our findings reveal the importance of evaluating models for determining properties of a gas mixture. Two of the gas mixture models available in the literature (Brokaw and Herning & Zipperer) compared well to experimental viscosity data. This contradicts results reported by Davidson who does not recommend the Herning and Zipperer method for hydrogen gas mixtures. The models from Davidson, Graham, and Wilke significantly underestimate the viscosity of the hydrogen mixtures investigated in this paper.

Fluidization characteristics and gas-solid heat transfer in a bubbling fluidized bed reactor can be greatly affected by the carrier gas properties. Based on our results, hydrogen gas requires approximately twice the flow rate of nitrogen gas to reach similar fluidization conditions in a BFB reactor. We also found that the thermal properties of the hydrogen gas improves its convective heat transfer capability thus increasing its potential to pyrolyze biomass compared

to a nitrogen gas environment. From our simulations, we found that the yield of bio-oil is independent of the carrier gas mixture when the flow rate is constant, with the average tar yield varying less than 2% across each of the mixtures investigated. Furthermore, by utilizing a low molecular weight gas such as H_2 while maintaining a constant U_s/U_{mf}, the bio-oil yields can be increased 7.7%. This is due to the lower density H_2 producing similar hydrodynamics as N_2 at higher gas flowrates. These higher flowrates result in shorter gas residence times, and as a result, less secondary reactions converting bio-oil to light gases and char.

7   Source code

Python code for calculating gas properties, fluidization characteristics, and for evaluating the pyrolysis kinetics is available on GitHub at `https://github.com/wigging/gas-effects-paper`. Functionality provided by the Chemics package was used for gas property and fluidization calculations. More information about Chemics is available at `https://chemics.github.io`.

References

[1] M. Asadullah et al. "Jute stick pyrolysis for bio-oil production in fluidized bed reactor". In: *Bioresource Technology* 99 (2008), pp. 44–50.

[2] Colomba Di Blasi. "Analysis of Convection and Secondary Reaction Effects Within Porous Solid Fuels Undergoing Pyrolysis". In: *Combustion Science and Technology* 90 (1993), pp. 315–340.

[3] Colomba Di Blasi and Carmen Branca. "Kinetics of Primary Product Formation from Wood Pyrolysis". In: *Industrial & Engineering Chemistry Research* 40 (2001), pp. 5547–5556.

[4] A.V. Bridgwater. "Principles and practice of biomass fast pyrolysis processes for liquids". In: *Journal of Analytical and Applied Pyrolysis* 51 (1999), pp. 3–22.

[5] Tony Bridgwater. "Challenges and Opportunities in Fast Pyrolysis of Biomass: Part I". In: *Johnson Matthey Technology Review* 62.1 (2018), pp. 118–130.

[6] Richard S. Brokaw. *Viscosity of Gas Mixtures*. NASA Technical Note NASA-TN-D-4496. NASA Lewis Research Center, 1968.

[7] Wai-Chun R. Chan, Marcia Kelbon, and Barbara B. Krieger. "Modelling and experimental verification of physical and chemical processes during pyrolysis of a large biomass particle". In: *Fuel* 64 (1985), pp. 1505–1513.

[8] A.P. Collier et al. "The heat transfer coefficient between a particle and a bed (packed or fluidised) of much larger particles". In: *Chemical Engineering Science* 59.21 (2004), pp. 4613–4620.

[9]   Thomas A. Davidson. *A Simple and Accurate Method for Calculating Viscosity of Gaseous Mixtures.* Tech. rep. Report of Investigations 9456. United States Department of the Interior, 1993.

[10]   Yaseen Elkasabi, Charles A. Mullen, and Akwasi A. Boateng. "Aqueous Extractive Upgrading of Bio-Oils Created by Tail-Gas Reactive Pyrolysis To Produce Pure Hydrocarbons and Phenols". In: *ACS Sustainable Chemistry and Engineering* 3.11 (2015), pp. 2809–2816.

[11]   Gary H. Ganser. "A rational approach to drag prediction of spherical and nonspherical particles". In: *Powder Technology* 77.2 (1993), pp. 143–152. DOI: https://doi.org/10.1016/0032-5910(93)80051-B. URL: http://www.sciencedirect.com/science/article/pii/003259109380051B.

[12]   Xi Gao et al. "Development and validation of an enhanced filtered drag model for simulating gas-solid fluidization of Geldart A particles in all flow regimes". In: *Chemical Engineering Science* 184 (2018), pp. 33–51. DOI: https://doi.org/10.1016/j.ces.2018.03.038. URL: http://www.sciencedirect.com/science/article/pii/S0009250918301726.

[13]   Dimitri Gidaspow. *Multiphase Flow and Fluidization: Continuum and Kinetic Theory Descriptions.* Academic Press, Inc., 1994.

[14]   Thomas Graham. "On the Motion of Gases". In: *Philosophical Transactions of the Royal Society of London* 136 (1846), pp. 573–631.

[15]   A Haider and O Levenspiel. "Drag coefficient and terminal velocity of spherical and nonspherical particles". In: *Powder technology* 58.1 (1989), pp. 63–70.

[16]   F. Herning and L. Zipperer. "Calculation of the Viscosity of Technical Gas Mixtures From the Viscosity of the Individual Gases". In: *Gas-und Wasserfac* 79 (1936), pp. 69–73.

[17]   Daniel Howe et al. "Field-to-Fuel Performance Testing of Lignocellulosic Feedstocks: An Integrated Study of the Fast Pyrolysis-Hydrotreating Pathway". In: *Energy & Fuels* 29 (2015), pp. 3188–3197.

[18]   A. Van Itterbeek, O. Van Paemel, and Miss J. Van Lierde. "Measurements on the Viscosity of Gas Mixtures". In: *Physica* 13.1-3 (1947), pp. 88–96.

[19]   Kwang Ho Kim, Robert C. Brown, and Xianglan Bai. "Partial oxidative pyrolysis of acid infused red oak using a fluidized bed reactor to produce sugar rich bio-oil". In: *Fuel* 130 (2014), pp. 135–141.

[20]   Daizo Kunii and Octave Levenspiel. *Fluidization Engineering.* 2nd ed. Chemical Engineering. Butterworth-Heinemann, 1991.

[21]   Liqiang Lu et al. "Bridging particle and reactor scales in the simulation of biomass fast pyrolysis by coupling Particle resolved simulation and coarse grained CFD-DEM". In: *Chemical Engineering Science* 216 (2020), p. 115471.

[22] Liqiang Lu et al. "EMMS-based discrete particle method (EMMS–DPM) for simulation of gas–solid flows". In: *Chemical Engineering Science* 120 (2014), pp. 67–87. DOI: https://doi.org/10.1016/j.ces.2014.08.004. URL: http://www.sciencedirect.com/science/article/pii/S0009250914004229.

[23] Ofei D. Mante et al. "The influence of recycling non-condensable gases in the fractional catalytic pyrolysis of biomass". In: *Bioresource Technology* 111 (2012), pp. 482–490.

[24] Pelle Mellin, Efthymios Kantarelis, and Weihong Yang. "Computational fluid dynamics modeling of biomass fast pyrolysis in a fluidized bed reactor, using a comprehensive chemistry scheme". In: *Fuel* 117 (2014), pp. 704–715.

[25] Dinesh Mohan, Charles U. Pittman, and Philip H. Steele. "Pyrolysis of Wood/Biomass for Bio-oil: A Critical Review". In: *Energy & Fuels* 20 (2006), pp. 848–889.

[26] Charles A. Mullen, Akwasi A. Boateng, and Neil M. Goldberg. "Production of Deoxygenated Biomass Fast Pyrolysis Oils via Product Gas Recycling". In: *Energy & Fuels* 27.7 (2013), pp. 3867–3874.

[27] Helio A. Navarro and Meire P. de Souza Braun. "Determination of the normal spring stiffness coefficient in the linear spring–dashpot contact model of discrete element method". In: *Powder Technology* 246 (2013), pp. 707–722. DOI: https://doi.org/10.1016/j.powtec.2013.05.049. URL: http://www.sciencedirect.com/science/article/pii/S0032591013004178.

[28] T.J.P. Oliveira, C.R. Cardoso, and C.H. Ataíde. "Bubbling fluidization of biomass and sand binary mixtures: Minimum fluidization velocity and particle segregation". In: *Chemical Engineering and Processing: Process Intensification* 72 (2013), pp. 113–121. DOI: https://doi.org/10.1016/j.cep.2013.06.010. URL: http://www.sciencedirect.com/science/article/pii/S025527011300158X.

[29] K. Papadikis, S. Gu, and A.V. Bridgwater. "Computational modelling of the impact of particle size to the heat transfer coefficient between biomass particles and a fluidised bed". In: *Fuel Processing Technology* 91 (2010), pp. 68–79.

[30] K. Papadikis et al. "Application of CFD to model fast pyrolysis of biomass". In: *Fuel Processing Technology* 90 (2009), pp. 504–512.

[31] Joseph P. Polin et al. "Conventional and autothermal pyrolysis of corn stover: Overcoming the processing challenges of high-ash agricultural residues". In: *Journal of Analytical and Applied Pyrolysis* 143 (2019), p. 104679.

[32] Joseph P. Polin et al. "Process intensification of biomass fast pyrolysis through autothermal operation of a fluidized bed reactor". In: *Applied Energy* 249 (2019), pp. 276–285.

[33] D.L. Pyle and C.A. Zaror. "Heat Transfer and Kinetics in the Low Temperature Pyrolysis of Solids". In: *Chemical Engineering Science* 39.1 (1984), pp. 147–158.

[34] Madhava Syamlal, William Rogers, and Thomas J. O'Brien. *MFIX Documentation Theory Guide*. Tech. rep. DOE/METC-94/1004. U.S. DOE Morgantown Energy Technology Center, Dec. 1993.

[35] Von Max Trautz and P.B. Baumann. "Die Reibung, Wärmeleitung und Diffusion in Gasmischungen. II. Die Reibung von H2-N2- und H2-CO-Gemischen". In: *Annalen der Physik* 394.6 (1929), pp. 733–736.

[36] Anna Trendewicz et al. "Evaluating the effect of potassium on cellulose pyrolysis reaction kinetics". In: *Biomass and Bioenergy* 74 (2015), pp. 15–25.

[37] C.R. Wilke. "A Viscosity Equation for Gas Mixtures". In: *The Journal of Chemical Physics* 18.4 (1950), pp. 517–519.

[38] Qingang Xiong et al. "Modeling the impact of bubbling bed hydrodynamics on tar yield and its fluctuations during biomass fast pyrolysis". In: *Fuel* 164 (2016), pp. 11–17.

[39] Q. Xue, T.J. Heindel, and R.O. Fox. "A CFD model for biomass fast pyrolysis in fluidized-bed reactors". In: *Chemical Engineering Science* 66.11 (2011), pp. 2440–2452.

[40] Carl L. Yaws. *Yaws' Critical Property Data for Chemical Engineers and Chemists*. Knovel, 2014.

[41] Huiyan Zhang et al. "Biomass fast pyrolysis in a fluidized bed reactor under N2, CO2, CO, CH4 and H2 atmospheres". In: *Bioresource Technology* 102 (2011), pp. 4258–4264.

[42] ZYa Zhou, AB Yu, and Paul Zulli. "Particle scale study of heat transfer in packed and bubbling fluidized beds". In: *AIChE Journal* 55.4 (2009), pp. 868–884.